Volume 17
Number 17
7 May 2021
Pages 4467–4666

Soft Matter

rsc.li/soft-matter-journal

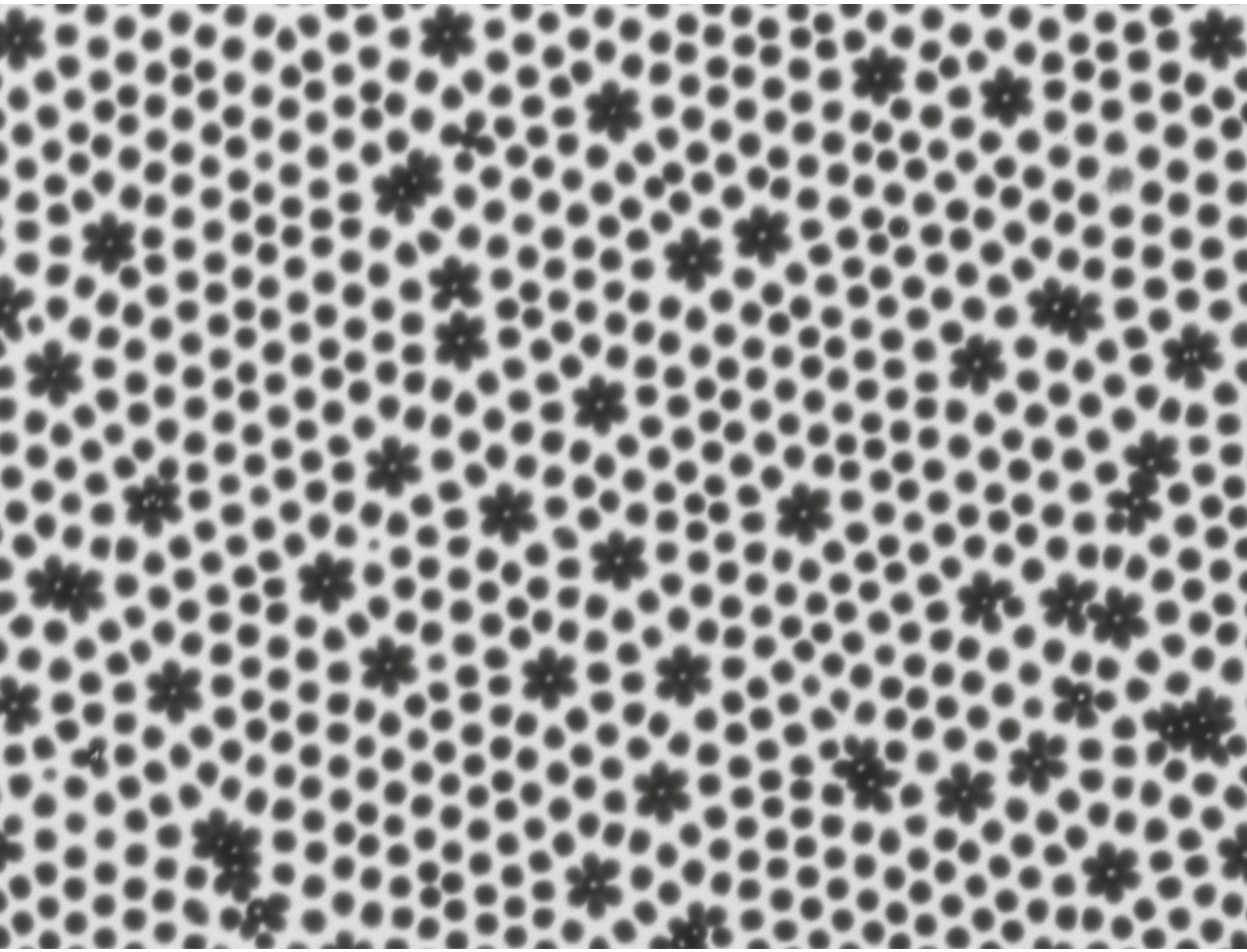

ISSN 1744-6848

ROYAL SOCIETY OF CHEMISTRY

PAPER
Liesbeth M. C. Janssen, Nicolas Vogel *et al.*
Collapse-induced phase transitions in binary interfacial microgel monolayers

Soft Matter

PAPER

View Article Online
View Journal | View Issue

Check for updates

Cite this: *Soft Matter*, 2021, **17**, 4504

Collapse-induced phase transitions in binary interfacial microgel monolayers†

Johannes Harrer,‡[a] Simone Ciarella,‡[b] Marcel Rey,[a] Hartmut Löwen,[c] Liesbeth M. C. Janssen*[b] and Nicolas Vogel*[a]

Microgels, consisting of a swollen polymer network, exhibit a more complex self-assembly behavior compared to incompressible colloidal particles, because of their ability to deform at a liquid interface or collapse upon compression. Here, we investigate the collective phase behavior of two-dimensional binary mixtures of microgels confined at the air/water interface. We use stimuli-responsive poly(*N*-isopropylacrylamide) microgels with different crosslinking densities, and therefore different morphologies at the interface. We find that the minority microgel population introduces lattice defects in the ordered phase of the majority population, which, in contrast to bulk studies, do not heal out by partial deswelling to accommodate in the lattice. We subsequently investigate the interfacial phase behavior of these binary interfacial assemblies under compression. The binary system exhibits three distinct isostructural solid–solid phase transitions, during which the coronae between two small particles collapse first, followed by the collapse between small–large and large–large microgel pairs. A similar hierarchy of phase transitions is found for mixtures of microgels and core–shell particles. Simulations based on augmented potentials qualitatively reproduce the experimentally observed phase transitions. We rationalize the presence of this hierarchy in phase transitions from differences in the interfacial morphology between the species: the larger coronae of softer (and therefore larger) microgels provide a higher resistance to phase transitions compared to the smaller coronae of the more crosslinked microgels and core–shell particles. The control of phase transitions *via* the molecular architecture further allows the formation of characteristic, flower-like defects by introducing particles with "weaker" coronae that are more prone to collapse with their neighboring particles. Our findings underline the dominating role of the corona for interfacial microgel assemblies, which acts as an energy barrier, shifting the collapse to higher surface pressures.

Received 1st March 2021,
Accepted 25th March 2021

DOI: 10.1039/d1sm00318f

rsc.li/soft-matter-journal

Published on 25 March 2021. Downloaded on 5/6/2021 2:20:36 PM.

Introduction

Colloidal particles are interesting model systems with which to fundamentally investigate self-organization phenomena. In contrast to atomic crystals, colloidal particles can often be described by simpler interaction potentials and their motion occurs on a much slower timescale. This allows the visualization of various atomistic phenomena, such as crystal nucleation,[1–3] lattice melting,[4,5] defects[6–9] and grain boundary formation,[10–12] or the formation of defined clusters.[13,14]

Confining particles to a liquid interface is a convenient way of probing self-assembly and phase behavior in two dimensions (2D).[15–18] The phase behavior of incompressible particles is predominantly governed by their interaction potentials, which can be repulsive or attractive depending on the nature of the liquid interface.[19] If the size polydispersity is sufficiently low, spherical colloidal particles are able to form 2D crystals with long-range order.[19] Depending on the balance of attractive capillary and van der Waals forces and electrostatic repulsion, the particles can either form close-packed, dense structures or non-close-packed lattices where the interparticle distance is maximized.[20]

Soft microgel particles, consisting of crosslinked polymer chains that swell in water exhibit a more complex self-assembly behavior since they can deform, adapt their shape and partially collapse.[21] In particular, while they are spherical in bulk, they deform at liquid interfaces under the effect of surface tension[22] and assume a core–corona morphology.[23–27] This leads to a more complex interaction potential and correspondingly, a richer phase behavior compared to incompressible particles.[25,28–33] At low

[a] *Institute of Particle Technology, Friedrich-Alexander University Erlangen-Nürnberg, Cauerstrasse 4, 91058 Erlangen, Germany. E-mail: nicolas.vogel@fau.de*
[b] *Soft Matter and Biological Physics, Department of Applied Physics, Eindhoven University of Technology, 5600 MB Eindhoven, The Netherlands. E-mail: l.m.c.janssen@tue.nl*
[c] *Institute for Theoretical Physics II: Soft Matter, Heinrich-Heine University Düsseldorf, D-40225 Düsseldorf, Germany*

† Electronic supplementary information (ESI) available. See DOI: 10.1039/d1sm00318f

‡ Johannes Harrer and Simone Ciarella contributed equally to this work.

This journal is © The Royal Society of Chemistry 2021

Published on 25 March 2021. Downloaded on 5/6/2021 2:20:36 PM.

surface pressure, corresponding to a large available area per particle, microgels typically assemble into a hexagonal non-close-packed phase, where the microgels are in corona–corona contact.[28] Upon compression, they typically undergo an isostructural phase transition into a hexagonal close-packed arrangement, where the microgels are in core–core contact,[24,28,29,33] but depending on their interfacial morphology, continuous[25,31,34,35] and heterostructural transitions[30,33] are also observed. The diameter each microgel assumes when adsorbed to the interface depends on its molecular architecture and is affected by its crosslinking density. Softer, less crosslinked microgels are able to deform more under the influence of surface tension and generally occupy larger areas.[31,36] The surface pressure at which the isostructural phase transition is induced similarly depends on the crosslinking density. More crosslinked particles undergo a phase transition more readily at lower surface pressures, because of the smaller extent of their corona.[31]

More complex assembly structures can result from the co-assembly of binary particle mixtures with different sizes. Incompressible particles can form ordered, binary assemblies only if their size is chosen in a way that the smaller particles fill up interstitial sites, both in 2D[37,38] and in 3D.[39–42] In contrast, if the size does not match, the system phase separates into two different incompatible crystal structures, or forms disordered structures if the phase separation is kinetically prevented, as is often the case in experiments.[8,43–47] The deformable nature of microgels, however, enables them to change their shape and size, which provides a pathway to form ordered lattices even with mismatching particle populations. As a specific example, it has been shown in bulk studies that larger microgels collapse to fit into the lattice formed by smaller particles and therefore heal out defects.[48–52]

Here, we study the phase behavior of binary mixtures of microgels at a liquid interface. We use microgels with a similar size in the collapsed state in the bulk, but different crosslinking densities, which translates into differences in their interfacial diameter due to their different deformability under the effect of surface tension. We observe a series of defined phase transitions, where the coronae of differently crosslinked particles collapse consecutively to form the hexagonally close-packed phase. These experimentally observed phase transitions are qualitatively reproduced by simulations based on augmented potentials, which capture multibody interactions between the different particle populations. These well-defined phase transitions allow the controlled formation of characteristic, flower-like defects by introducing particles with "weaker" coronae that are more prone to collapse with their neighboring particles. Interestingly, we do not observe any signs of crystal self-healing effects, where one population collapses to fit into the lattice provided by the second population, as observed in three dimensions.

Experimental

Materials

All chemicals were obtained from commercial sources and used as received if not otherwise stated. *N*,*N*′-Methylenebis(acrylamide) (BIS; 99%, Sigma-Aldrich), ethanol (99.9%, Sigma-Aldrich), ammonium persulfate (APS; 98% Sigma-Aldrich), tetraethyl orthosilicate (TEOS; 98%, Sigma-Aldrich), hexane (≥99%, Sigma-Aldrich), ammonium hydroxide solution (28–30% NH_3 basis, Sigma-Aldrich) and (3-(trimethoxysilyl)propyl methacrylate) (MPS; 98%, Sigma-Aldrich) were used as received. *N*-Isopropylacrylamide (NiPAm; 97%, Sigma-Aldrich) was purified by recrystallization from hexane (95%, Sigma-Aldrich). Water was double deionized using a Milli-Q system (18.2 MΩ cm, Elga PURELAB Flex).

Microgel synthesis

All microgels and core–shell particles were synthesized by precipitation polymerization following literature protocols.[53,54] The poly(*N*-isopropylacrylamide) (PNiPAm) microgels had a cross-linker content of 2.5 mol% and 5 mol% of BIS with respect to the monomer NiPAm. They were synthesized in a one-pot surfactant-free precipitation polymerization. In short, 2.83 g of NiPAm and 94 mg/193 mg BIS in 249 mL of Milli-Q water was degassed with nitrogen and heated under stirring to 80 °C. Subsequently, 14.3 mg of APS was added and the reaction was continued for 5 h. The resulting microgels were purified by centrifugation and dialysis.[54] A similar synthesis scheme was adopted for the core–shell particles.[53] Silica cores (d = 160 nm) functionalized with (3-(trimethoxysilyl)propyl methacrylate, MPS) were synthesized *via* the Stöber process.[55] 3.767 g of an aqueous dispersion of these core particles (6.59 wt%) was added to a heated solution (80 °C) of 2.83g of NiPAm and 19.3 mg of BIS (corresponding to 5 mol% crosslinker) in 46 mL of Milli-Q water. One hour after the initiation of the reaction with 114 mg of APS, the same amount of APS was added again and a solution of 2.037 g NiPAm and 43 mg of BIS in 9 mL of Milli-Q water was continuously fed into the reaction over a period of 3 h at a rate of 3 mL h^{-1}. After an additional 2 h of reaction time, the dispersion was cooled and purified by centrifugation and dialysis.

Interfacial characterization

The interfacial phase behavior of the microgels was investigated using a Langmuir–Blodgett trough (KSV Nima) with ultrapure Milli-Q water as a sub-phase. A 0.025 wt% dispersion of microgels with varying ratios of two different populations in a 1 : 1 ethanol/water mixture was spread at the air/water interface to create the initial monolayer. The interfacial assemblies were simultaneously compressed at 4 mm min^{-1} and deposited onto a silicon wafer (6 × 0.5 cm^2), which was mounted at 45° to the dipper and lifted through the air/water interface at a speed of 0.8 mm min^{-1}.[28,29] Using this procedure, the surface pressure and particle arrangement at the liquid interface can be correlated with a location on the substrate. Thus, the entire phase behavior under compression can be recorded on a single solid substrate and be subsequently investigated *ex situ*.[28,29] The transferred microgel monolayer on the solid substrate was characterized by scanning electron microscopy (SEM) (Zeiss Gemini 500) and atomic force microscopy (AFM) (JPK Nano Wizard, cantilever Anfatec NSC 18). The AFM images were post-processed and analyzed using Gwyddion. The SEM images were analyzed using a custom-written image analysis software,

Published on 25 March 2021. Downloaded on 5/6/2021 2:20:36 PM.

which is described in detail in our previous work.[56] The radial distribution function (RDF) was obtained by image analysis using ImageJ. For each ratio in Fig. 2 at least 15.000 particles in the corona-corona regime were examined. The bond orientational parameter Ψ_6 was used to characterize the local hexagonal structure around the particles and was calculated according to eqn (1), where N_b is the number of nearest neighbors and θ_j is the bond angle between the observed particle and its nearest neighbor j.

$$\Psi_6 = \left\langle \frac{1}{N_b} \left| \sum_{j=1}^{N_b} \exp(6i\theta_j) \right| \right\rangle \quad (1)$$

Simulations

To model the phase behavior of the microgels at the interface, we used the recently developed augmented ensemble approach.[33] In this approach, we represent the microgel particles simplistically as spheres with pairwise interactions in the form of a modified Lennard-Jones potential:

$$V(r_{ij}, \sigma_{ij}) = \begin{cases} 6\varepsilon \left[\left(\frac{\sigma_{ij}}{r_{ij}}\right)^{12} - \left(\frac{\sigma_{ij}}{r_{ij}}\right)^{6} + \sum_{l=0}^{3} c_{2l} \left(\frac{r_{ij}}{\sigma_{ij}}\right)^{2l} \right], & \text{if } \frac{r_{ij}}{\sigma_{ij}} < x_c \\ 0, & \text{if } \frac{r_{ij}}{\sigma_{ij}} > x_c \end{cases} \quad (2)$$

with an attractive energy well of depth ε. The coefficients c_{2l} are determined by requiring that the first three derivatives of V vanish at the adimensional cutoff distance $x_c = 2$. The parameter σ_{ij} is the sum of the radius σ_i of particle i and the radius σ_j of particle j. If σ_{ij} is large then the pair is widely spaced, corresponding to expanded corona–corona contact. If σ_{ij} is decreased the interparticle distance decreases, mimicking the collapse of the corona and the formation of a core–core contact. Note that the size difference between a 5% and a 2.5% cross-linked microgel in the simulation is embedded in the value of σ_{ij}, so all the species are modeled using the same interaction potential.

The cornerstone mechanism of the augmented ensemble approach is to let σ_{ij} evolve over time as an augmented variable, simultaneously with particle positions and momenta; the value of σ_{ij} captures the compression of each particle. The dynamics of σ_{ij} are coupled to the positions *via* the pairwise potential since V is dependent on σ_{ij},[33] producing a force that acts on σ_{ij} that depends on V. However, to confine the augmented variables in a physical regime, we added an external augmented potential $V_A(\sigma_{ij})$ that acts only on the augmented variables:

$$V_A^{\alpha\beta}(\sigma_{ij}^{\alpha\beta}) = K^{\alpha\beta}\left[(\sigma_{ij}^{\alpha\beta}\sigma_0^{\alpha\beta})^4 \Delta^{\alpha\beta}\right]^2 5K\Delta^{\alpha\beta}(\sigma_{ij}^{\alpha\beta}\sigma_0^{\alpha\beta}) \quad (3)$$

which is based on a double well potential with a barrier height of $\Delta^{\alpha\beta}$. Note that the indices α, $\beta = \{1, 2\}$ correspond to the 2.5 mol% and the 5 mol% microgels, respectively, so parameters with a superscript 11 correspond to a pair of 2.5 mol% microgels, superscript 22 corresponds to a pair of 5 mol% microgels, while superscript 12 is the interaction between a 2.5% with a 5% particle. The value of $\sigma_0^{\alpha\beta}$ controls the position of the two minima $\sigma_{+-}^{\alpha\beta} = \sigma_0^{\alpha\beta} \pm \sqrt{\Delta}$, while the linear term coefficient $5K\Delta^{\alpha\beta}$ is chosen such that the energy difference between the two minima is 10 times greater than the energy barrier, as explained in our previous work.[33] It follows that configurations with $\sigma_0^{\alpha\beta} = \sigma_-^{\alpha\beta}$ are disfavoured unless the compression is large. Furthermore, $K^{\alpha\beta}$ represents the magnitude of the potential, including the depth of the wells and barrier height. This serves as a qualitative measure to represent the overall stiffness of the particles. In Fig. S1 (ESI†) we show how the augmented potential is affected by the variation in Δ and K. Finally, as explained in ref. 33, the augmented ensemble can capture multi-body interactions by correlating the augmented variables of neighboring pairs, which are required to model the isostructural regime. Such multi-particle correlations are phenomenologically included in the model through the parameter λ_m.[33] These multi-body interactions effectively facilitate additional collapse events around a microgel pair that is already collapsed. From a molecular point of view, this behavior can be rationalized by assuming that collapse of a corona of a microgel in one direction also weakens the corona in the other directions, since the polymer chains in the microgels are connected *via* crosslinking points.

Microgel microgel mixture

The specific values of the simulation parameters were chosen to reproduce the experimental features of the microgel particles. While modeling pure microgel mixtures (Fig. 5) we first set the size of the two microgels to be: $\sigma_+^{11} = 1.14$ μm and $\sigma_-^{11} = 0.34$ μm for the large microgels (2.5 mol% crosslinkers) and $\sigma_+^{22} = 0.94$ μm and $\sigma_-^{22} = 0.34$ μm for the small microgels (5 mol% crosslinkers), as extracted from experimental data (Fig. 4). From these values we can calculate the corresponding σ_0 and Δ. The mixed terms Δ^{12} and σ_0^{12}, which are symmetric, average between the pure values of the 2.5 mol% (superscript 11) and the 5 mol% (superscript 22) microgels. We then set the stiffness prefactor $K^{11} = 10$ $K^{22} = 0.001$ $[L]^{-8}$ to qualitatively reproduce the experimental area per microgel. We reproduced the experimental compression by reducing the available area per microgels in the simulation scheme.

Core–shell microgel mixture

For the second mixture consisting of core–shell particles and 2.5% microgels (Fig. 7) we selected the parameters differently in an effort to qualitatively capture the flower-like defects observed in experiment. However, while the microscopic images clearly show flower-like defects for these mixtures (Fig. 6c and g), it proved more difficult to create such structures in simulation. We attribute this difficulty to the lack of many-body interactions in our simulations, as explained in Fig. S2 (ESI†). Briefly, any additional petal of the flower-like defect has to overcome the energy barrier required to get close not only to the particle at the center of the flower, but also to all of the other petals. To partially recreate flower-like defects in our simulation scheme, we increased the effect of many-body interactions by increasing λ_m to a value of 1.1 (as compared to $\lambda_m = 1.01$). As explained in ref. 33 and the section above, this parameter

 This journal is © The Royal Society of Chemistry 2021

Published on 25 March 2021. Downloaded on 5/6/2021 2:20:36 PM.

facilitates the collapse of particles that are already involved in a collapse, thus facilitating the formation of additional petals. Furthermore, we found that an optimal way to get a qualitative agreement with the experimentally observed structures is to calculate Δ and σ_0 by imposing that the expanded size $\sigma_+^{11} = \sigma_+^{22}$ corresponds to a perfect hexagonal lattice spacing at the lowest experimental compression, where the superscript 1 represents the 2.5% microgel and superscript 2 the core–shell particles. At the same time we set the collapsed sizes to be $\sigma_-^{11} = \frac{2}{3}\sigma_-^{22}$, thus fixing all the $\Delta^{\alpha\beta}$ and $\sigma_0^{\alpha\beta}$ values. Finally, since the core–shell particles are the first ones to collapse in the experiments, we set $K^{22} = 0.1$ and $K^{11} = 0.004$ nm^{-8}, thus artificially reducing the energy required for the core–shell particles to reach the collapsed configurations. This qualitatively captures the experimental behavior, where the core–shell particles collapse at lower surface pressures compared to the pure microgels.[53]

Computational details

We performed 2D molecular dynamics (MD) simulations with periodic boundary conditions to represent the interfacial layer on which our mixtures are absorbed. First, the interfaces are equilibrated in a canonical *NVT* ensemble, at a constant particle number of $N = 500$ and temperature T; where the volume $V = L^2$ is our control parameter, expressed in units of $[L] = 100$ nm, which we reduce to increase the compression by reducing the area per particle A_p. We used the leap-frog integration method and a Berendsen thermostat to keep the temperature T constant during the initial equilibration.[57] We set the mass of each particle as our unit $m = M$. Each interface was equilibrated for 10^5 time steps of size $dt = 5 \times 10^{-4}\,[M]^{1/2}[L][\varepsilon]^{-1/2}$ reduced units at $T = 2[\varepsilon]$ and large A_P.

We then induced a compression by reducing A_p through L. During the compression, the experimental systems are in a quenched state where there are no thermal fluctuations. We mimicked this feature by replacing the thermostat with the FIRE algorithm[58] to minimize the energy and find the inherent structure at target A_P.

While the specific units to model each particle type are reported in the previous sections, there are some parameters that were kept constant for all the different mixtures: for the many-body interactions we used $\lambda_m = 1.01$, which has shown to be a good value to model the isostructural regime;[33] we set the augmented mass of all the particles to be equal to the mass $m_{\sigma m} = m = 1[M]$ because the effects due to relative inertia are already embedded in the parameter K.

Finally, we repeated the procedure for $M > 50$ randomly generated configurations in order to verify the consistency of the results and improve the statistics.

Results

We investigated the phase behavior of binary microgel mixtures consisting of two PNiPAm microgel populations with different crosslinking densities during compression on a Langmuir trough and transfer to a solid substrate.[28,29,54] We chose microgel populations that exhibited similar hydrodynamic diameters in the collapsed state in bulk (Fig. S3, ESI†) as well as comparable interfacial diameters when collapsed into core–core contact in the hexagonal close-packed phase at high surface pressures (d_{col} = 340 nm).[54] At lower surface pressures (<16 mN m^{-1}), however, when the microgels exist in their characteristic core–corona morphology, their interfacial diameter differs,[54] as seen in the AFM phase images (Fig. 1a–c) and in statistical evaluations of the average nearest neighbor distance in the SEM images after transfer to a solid substrate (Table 1). Microgels with 2.5 mol% crosslinking density occupied an area per particle of 1.0 μm^2, and had a nearest neighbor distance of 1130 nm at a surface pressure of 15 mN m^{-1}.[54] In the following, this population is labelled as "large". Microgels with 5 mol% crosslinking density occupied an area per particle of 0.65 μm^2, and had a nearest neighbor distance of 910 nm at 15 mN m^{-1}.[54] This population is subsequently labelled as "small". First, we focus on mixtures between these two microgel populations while the core–shell particles, seen in Fig. 1c, will be introduced later.

We first investigated the properties of the interfacial assemblies of the binary microgel mixtures at low surface pressure before the onset of any phase transition (<16 mN m^{-1}). We transferred the

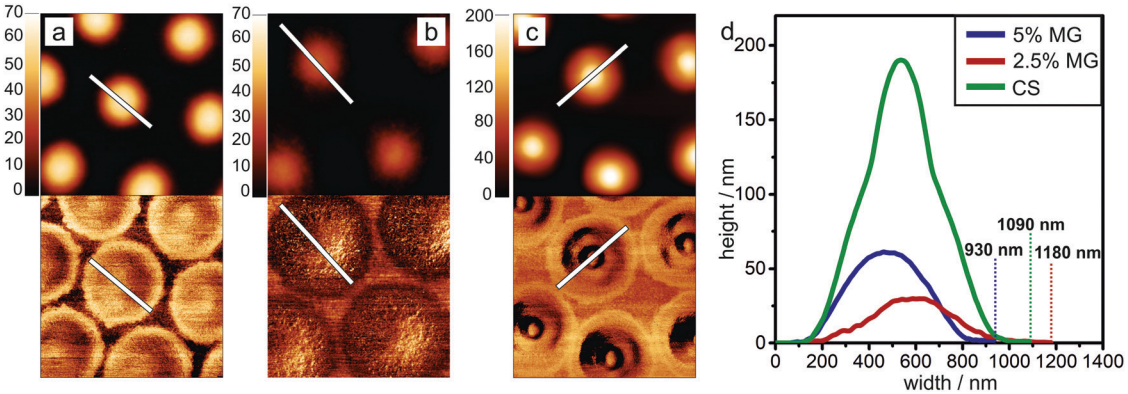

Fig. 1 AFM images and height profiles of the particles used in this study at a surface pressure of 1 mN m^{-1}. (a–c) AFM height (top) and phase (bottom) images of microgels with 5% crosslinker (a), 2.5% crosslinker (b)[56] and core shell particles with a 160 nm core and 5% crosslinking density (c). (d) Height profiles of microgels with 5% crosslinker (5% MG), 2.5% crosslinker (2.5% MG) and core shell particles (CS). Images: 2 × 2 μm^2.

Published on 25 March 2021. Downloaded on 5/6/2021 2:20:36 PM.

Table 1 Corona diameter seen in the AFM phase images at a surface pressure of 1 mN m^{-1} and average nearest neighbor distance measured by SEM at a surface pressure of 15 mN m^{-1}

	5% Crosslinked microgel	2.5% Crosslinked microgel	Core–shell particle
AFM corona diameter/nm	930	1180	1090
SEM nearest neighbor distance/nm	910	1130	1100

interfacial assembly to a solid substrate and used SEM to image the binary monolayer (Fig. 2, left column). We performed a Voronoi tessellation and visualized defects in the lattice using color-coding microgels with five or seven neighbors in blue and red, respectively (Fig. 2, second column). We then quantified the local order by calculating the Ψ_6 parameter of each microgel according to eqn (1) (Fig. 2, third column). A Ψ_6 parameter of 1 refers to perfect hexagonal order, whereas defects lead to a decrease in the Ψ_6 value. Finally, we assessed the global order over the entire image by averaging the Ψ_6 parameters, determining the fraction of microgels in defects and averaging the numbers of neighbors over the entire image (Fig. 2, right). In this procedure, we also distinguish between the different values for the individual populations of small and large

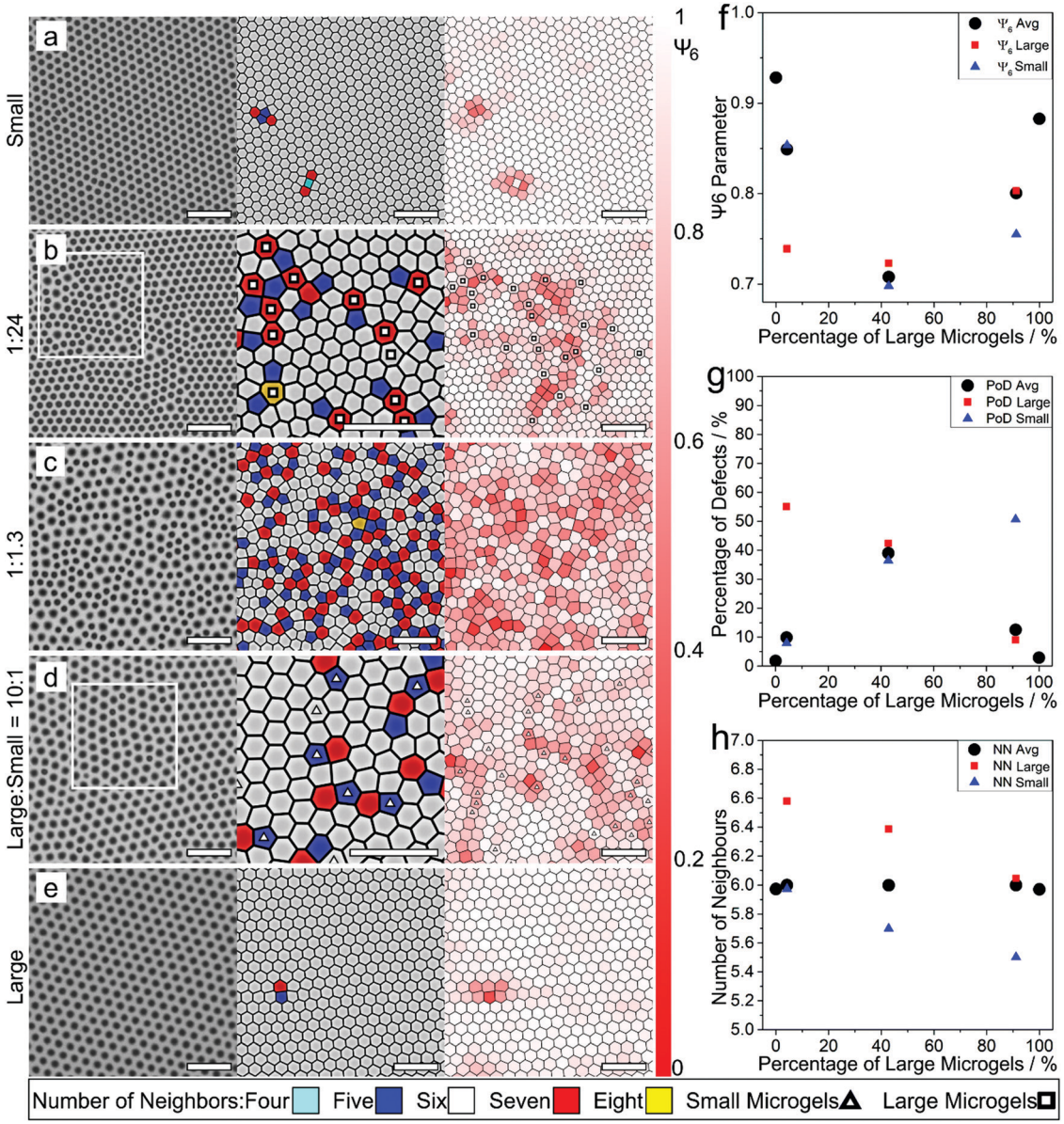

Fig. 2 Statistical image analysis of binary microgel arrays. (a–e) SEM images ((1) column) and the corresponding Voronoi tessellations highlighting defects ((2) column) and the Ψ_6 parameter ((3) column) of a microgel array consisting of small and large particles at different mixing ratios. (f) The Ψ_6 parameter as a function of the percentage of large microgels. The Ψ_6 parameter decreases when the mixing ratio approaches 1 : 1. (g) Percentage of defects as a function of the percentage of large microgels, which increases when the mixing ratio approaches 1 : 1. (h) Number of neighbors as a function of the percentage of large microgels. Larger particles have on average more than six neighbors in binary mixtures. Scale bar: 4 μm.

 This journal is © The Royal Society of Chemistry 2021

Published on 25 March 2021. Downloaded on 5/6/2021 2:20:36 PM.

microgels, to assign their individual contributions to order and defects within the binary lattice.

Both the individual populations of either small or large microgels formed hexagonal non-close packed lattices at the air/water interface, which are characterized by a high degree of order and few defects (Fig. 2a and e). The large microgels had an average Ψ_6 value of 0.88 and only 2.8% were assigned as defects, while the small microgels have an average Ψ_6 value of 0.93 with a number of defects of 1.8% (Fig. 2f–g). The average number of neighbors was 6.0 for both pure microgels, corroborated with the high order of the interfacial assembly (Fig. 2h).

Next, we formed binary assemblies with a number ratio of large/small = 1 : 24, corresponding to 4% of large microgels, which is close to the ratio in the bulk that exhibited self-healing properties by deswelling of the larger minority population to fit into the crystal lattice of the small microgels.[48–52] At surface pressures below the phase transition (<16 mN m^{-1}), however, no local size-reduction of the large microgel population to form an ordered binary lattice was observed (Fig. 2b). Instead, the large microgels formed defects and locally distorted the lattice of the smaller particles. On average, they had 6.6 nearest neighbors (Fig. 2h). As a result, the average Ψ_6 parameter of the binary assembly dropped to 0.85 (Fig. 2f) and the percentage of defects increased to 10% (Fig. 2g). A comparable behavior was observed for binary assemblies with a majority population of the large microgels (number ratio large/small = 10 : 1) (Fig. 2d). In this case, the small microgels formed local defects within the lattice of the large microgels and therefore exhibited a low order parameter (0.75, Fig. 2f). Due to their smaller size, their average number of neighbors reduced to 5.5 (Fig. 2h). As a consequence, the global order decreased, as indicated by an average Ψ_6 parameter of 0.81 (Fig. 2f), with an average of 13% defects (Fig. 2g).

Binary assemblies with close to equal ratios of large and small microgels (Fig. 2c) were not able to form an ordered lattice. In this case, we observed a disordered arrangement with a low Ψ_6 parameter of 0.71 (Fig. 2f) and a high number of defects (40%, Fig. 2g). The large microgels had an average of 6.4 neighbors and the small ones an average of 5.7 neighbors (Fig. 2h).

These experiments show that the microgels at the interface retained their individual interfacial dimensions without adapting their size to form an ordered lattice. This contrasts bulk behavior, where Scotti *et al.* showed that defects induced by larger individual microgels self-heal completely and form ordered lattices even for mixtures with 6.6% of large particles and a size ratio of 0.67.[49] Apparently, the extended coronae at the interface provide an energy barrier towards collapse that exceeds the gain in energy to form an ordered lattice.

We further characterized the 2D lattices of the different interfacial assemblies using the radial distribution function averaged over all species (RDF). The RDF of pure small microgels (Fig. 3a) shows the basic characteristics of a hexagonal arrangement with long-range order. The first and highest peak corresponds to the nearest neighbors of any particle in the lattice, while the second and third peaks are clearly separated and correspond to the second ring surrounding the central particle. The RDF exhibits several consecutive peaks, corresponding to a correlation of order over longer ranges, extending up to seven nearest neighbor distances. In contrast, the RDF of the binary microgel assembly with a large/small ratio of 1 : 1.3 shows a decrease in long-range order with fewer and less defined peaks (Fig. 3b). Interestingly, however, the peak corresponding to the nearest neighbors shows defined splitting (Fig. 3c). The three sub-features that can be distinguished can be clearly correlated to the different interparticle distance between small–small, small–large and large–large microgels. In the next part, we will see how these different nearest neighbor pairs govern the phase behavior of the binary microgel layers upon compression.

Next, we investigated the phase behavior of the microgels upon compression of the interface, which leads to a decrease in the available area per particle and an increase in surface pressure.[28,29] The compression is reflected by the increase in

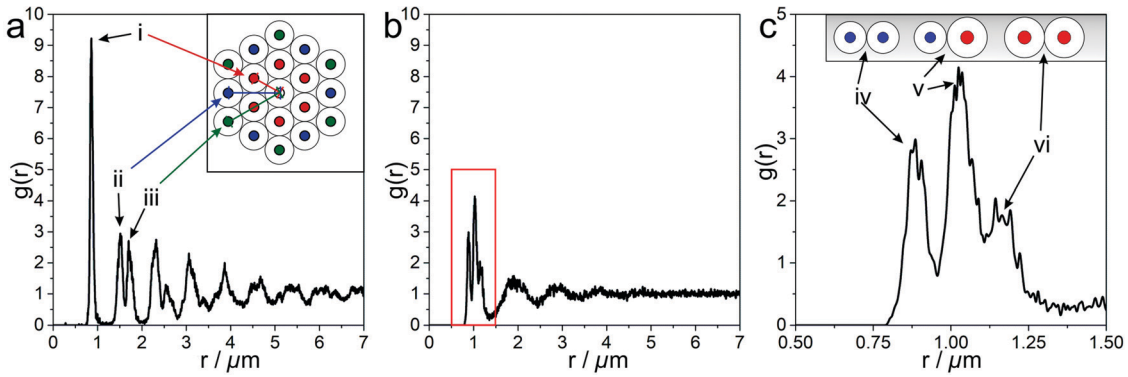

Fig. 3 RDF of pure and mixed microgel arrays. (a) RDF of a microgel array consisting only of small particles. Narrow peaks and long-range order can be observed. The first three peaks correspond to the distance between (i) nearest neighbors, (ii) second nearest neighbors and (iii) third nearest neighbors. (b) RDF of a microgel array consisting of a mixture of large and small particles in a ratio of 1 : 1.3. Broad peaks and the absence of a long-range order can be observed. (c) Enlarged first peak of (b) with a schematic representation of neighboring particles. Three peaks can be observed, which peaks correspond to the distance between (iv) small–small, (v) small–large and (vi) large–large particles.

Published on 25 March 2021. Downloaded on 5/6/2021 2:20:36 PM.

the surface pressure of the microgels. As the difference between the extended and compressed state is smaller for smaller microgels, their compression isotherm is steeper compared to their large counterparts.[31] As expected, the compression isotherm of a 1 : 1 mixture of both species was in between the curves of the pure microgels, as seen in Fig. S4 in the ESI.† Upon compression, the microgels undergo an isostructural solid–solid phase transition from a hexagonal non-close packed phase where the individual microgels are in corona-corona contact to a close-packed phase with core-core contact.[31] The onset of this phase transition depends on the crosslinking density.[54] For larger, less-crosslinked microgels the phase transition starts at 27 mN m^{-1}, while the smaller, more crosslinked microgels exhibit a phase transition at 19 mN m^{-1}.[54] In the binary system, we expect a competition between the decreased tendency of individual larger microgels to undergo the phase transition and the gain energy obtained from forming a defect-free hexagonal lattice upon collapse of the larger particles.[48–52]

Fig. 4 shows the phase behavior of binary microgel monolayers with different compositions as a function of the surface pressure. All of the binary systems showed a series of three consecutive phase transitions, which can be related to the collapse of the different nearest neighbor pairs identified in Fig. 4. For all of the different mixing ratios, below a surface pressure of 18 mN m^{-1} (Fig. 4a, e, i and m), both microgel populations remained in corona–corona contact without noticeable rearrangement of the interfacial assembly. Above 19 mN m^{-1}, which is the onset of the phase transition for pure small microgels,[54] the small microgels in contact with other small microgels underwent a phase transition into a hexagonal close-packed structure with core–core contact. At this surface pressure, the large, less-crosslinked microgels were still separated from their

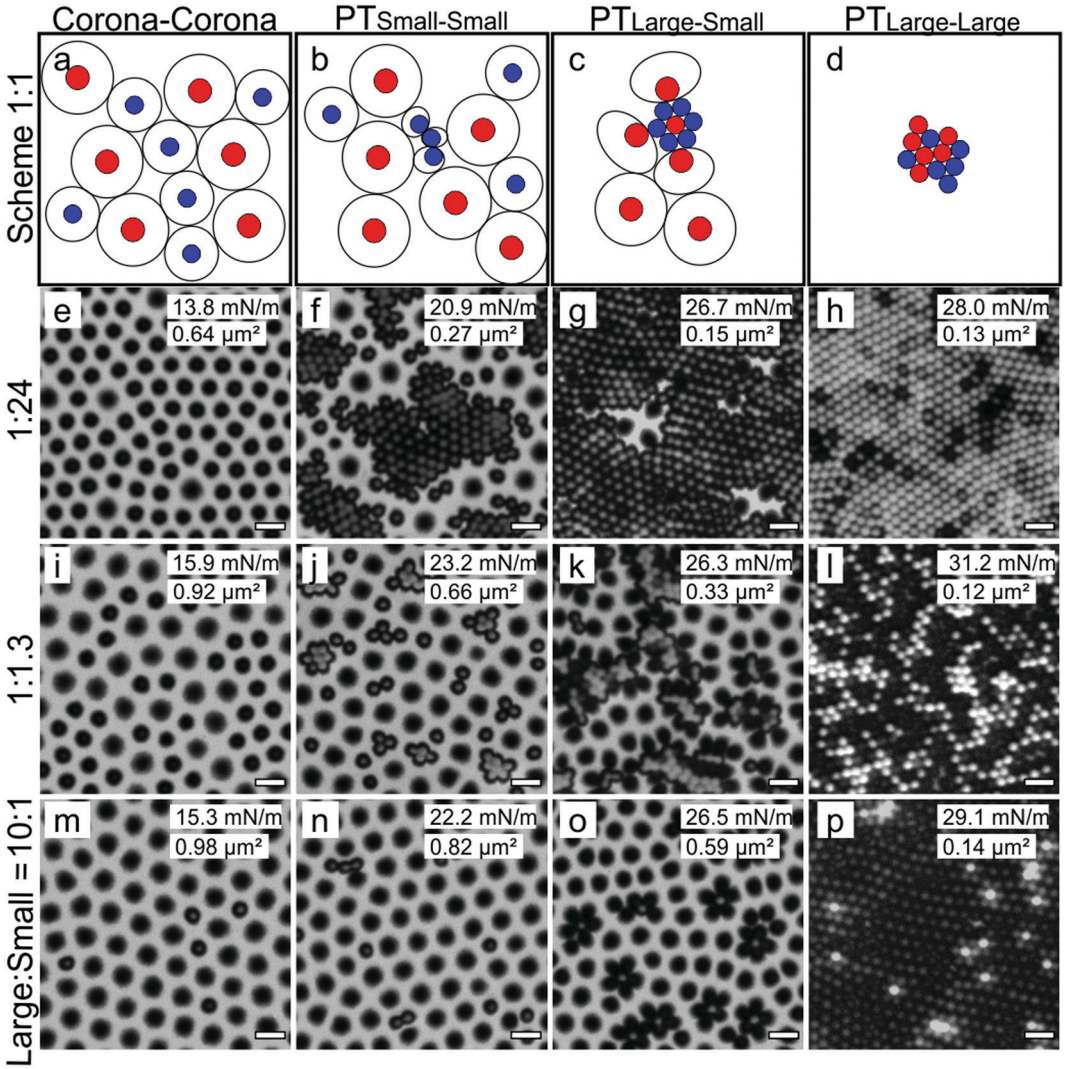

Fig. 4 Interfacial phase transition of binary microgel mixtures at different mixing ratios of large and small particles. "Small" microgels had 5 mol% crosslinker, "large" microgels" had 2.5 mol% crosslinker. (a–d) Schematic representation of the series of phase transition in binary mixtures of more (red) and less (blue) cross-linked microgels. Four phases with three phase transitions can be distinguished. (e–h) SEM images of the phase transition in a monolayer with 4% of large particles. (i–l) SEM images of the phase transition in a monolayer with 43% of large particles. (m–p) SEM images of the phase transition in a monolayer with 91% of large particles. Surface pressure and particle area are displayed for each SEM image. Scale bars: 1 µm.

 This journal is © The Royal Society of Chemistry 2021

Published on 25 March 2021. Downloaded on 5/6/2021 2:20:36 PM.

neighbors *via* their extended corona. Similarly, small microgels in contact with large microgels remained in corona–corona contact (Fig. 4b, f, j and n). We therefore denote this phase transition as $PT_{small-small}$. At a surface pressure of 25 mN m^{-1}, a second phase transition occurred, where the nearest neighbors of the large and small microgels collapsed into core–core contact (Fig. 4c, g, k and o). We denote this phase transition as $PT_{large-small}$. This phase transition produces characteristic, flower-like structures, especially when small microgels are the minor component and are therefore predominantly surrounded by large microgels (Fig. 4o).[54] At 28 mN m^{-1} we observed the third phase transition, that occurs between neighboring large microgels, denoted as $PT_{large-large}$ (Fig. 4d, h, l and p). After this phase transition, a complete, hexagonally close packed state was formed. Since both large and small particles have a similar hydrodynamic diameter in the collapsed state at 50 °C (Fig. S3, ESI†), they also have a similar size when in core–core contact. Thus, the order of the hexagonal close packed lattice of the binary mixtures is higher compared to that of a non-close packed lattice. In the case of a mixing ratio of 1 : 1.3 (or, 43% of large particles) (Fig. 4i–l), the close packed state has 5% defects (Fig. S5b, ESI†) compared to 40% in the non-close packed state (Fig. 2c).

We correlated the experimental observations with our augmented-ensemble computer simulations,[33] which, due to the incorporation of multi-body interactions, can also reproduce the isostructural phase transitions.[33] Fig. 5 shows snapshots of the simulations during the compression process. To simplify visualization, the larger, less crosslinked microgels are represented as red spheres that turn yellow upon collapse, while the smaller, more crosslinked microgels are represented as grey spheres that turn blue upon collapse. We analysed the three different compositions used in the experiment: a system with a large number of small microgels (Fig. 5a–d) corresponding to Fig. 4e–h, a near-equal mixing ratio (Fig. 5f–i, corresponding to Fig. 4i–l), and a system with a large microgels as the majority population (Fig. 5k–n, corresponding to Fig. 4m–p). The augmented potential simulation method qualitatively reproduces all different experimentally observed phases. We further analyzed the fraction of each type of microgel in the collapsed state at the given compression (Fig. 5e, j and o). At low compression, all microgels are predominantly in corona-corona contact (Fig. 5a). With increasing surface pressure, first small microgels in contact with small microgels collapse into close contact (visualized by a change from grey to blue), while the large microgels remain (visualized by the prevalence of red particles). This phase transition corresponds to the $PT_{small-small}$ phase transition observed in the experiments (Fig. 4, second column). With increasing compression, large microgels collapse exclusively with neighboring

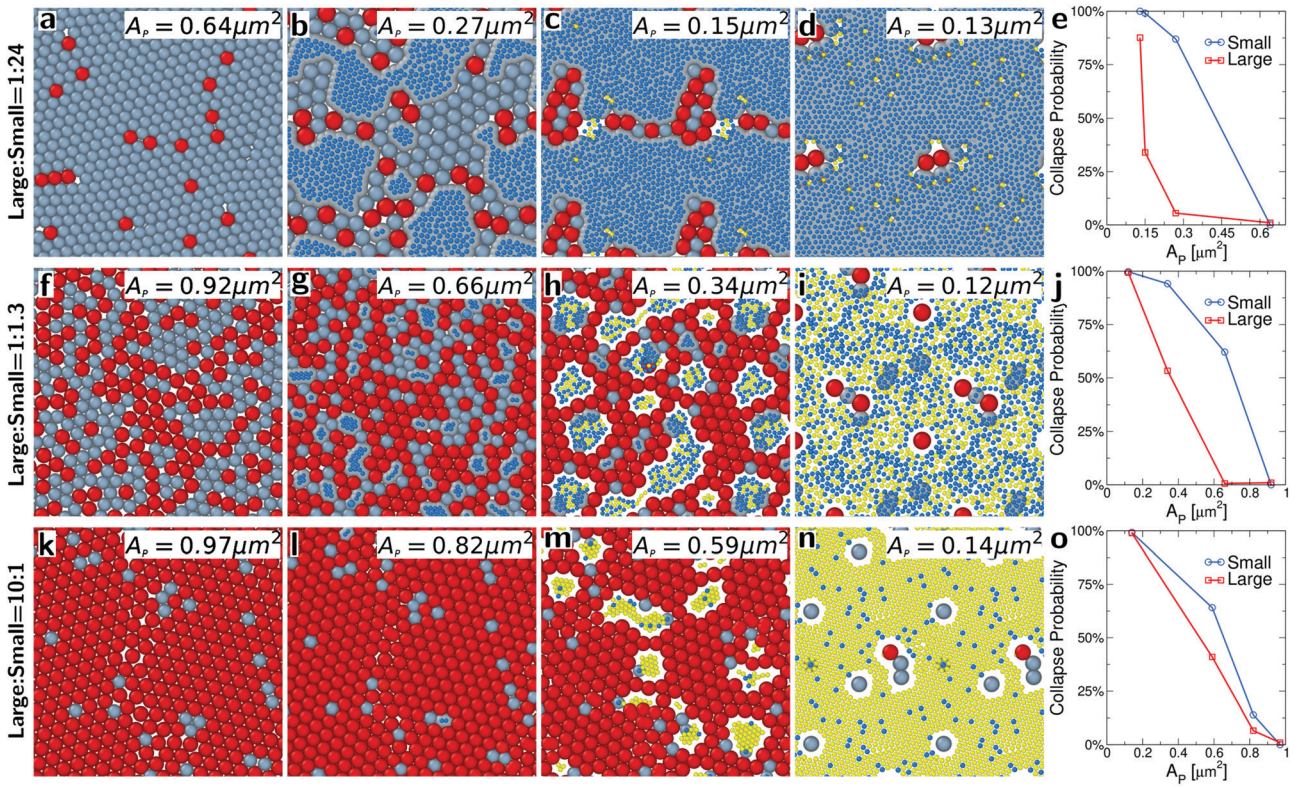

Fig. 5 Phase transitions of binary microgel mixtures in 2D simulations using the augmented ensemble technique. The larger, less crosslinked microgels are represented as red spheres that turn yellow if collapsed. The smaller, more crosslinked microgel are represented as grey spheres that turn blue upon collapse. (a–d), (f–i) and (k–n) Snapshots of the simulations corresponding to different mixing ratios of both populations as indicated in the panels. The image series in the individual columns show increasing compressions to the same area per microgel as in the experiment. Overall, the four phases (corona–corona, small–small, small–large and large–large) observed in the experiments are reproduced by the simulations. (e, j and o) Statistical evaluations of the simulation snapshots showing the percentage of collapsed microgels in both populations as a function of the area per particle.

Published on 25 March 2021. Downloaded on 5/6/2021 2:20:36 PM.

small microgels, particularly when all their neighbors are small, reproducing the $PT_{large-small}$ phase transition (Fig. 4, third column). Finally, at the highest compression, the large microgels collapse with neighboring large microgels (corresponding to the $PT_{large-large}$ phase transition), forming a close packed binary phase (Fig. 4, fourth column).

In the experiments discussed so far, the microgels were chosen to produce similar interfacial diameters in the compressed state but had different interfacial diameters in the expanded state. Next, we investigated the phase behavior in the opposing case, *i.e.* using a binary mixture with similar interfacial diameters in the expanded state but different interfacial diameters in the compressed state. In this set of experiments, we replaced the small microgels with core–shell particles and formed binary monolayers using the large microgel population from above as the major component (Fig. 6). The core–shell particles contained a silica core and a PNiPAm shell with interfacial dimensions that matched those of the large microgels in the expanded state. The presence of the stiff silica core increases the interfacial attraction *via* capillary forces and facilitates the interfacial collapse into a close-packed phase.[53] The core–shell particles thus require a lower surface pressure to trigger phase transition. We therefore use the subscript "low" to assign their phase transitions in Fig. 6. Concurrently, we use the subscript "high" to describe the phase transition of the pure microgels due to their higher transition threshold. At low surface pressure, the binary mixtures formed an ordered hexagonal non-close packed lattice arrangement where the core–shell particles fitted into the lattice of the microgels, as expected from the similar expanded diameter (Fig. 6a and e). When compressed above a surface pressure of 15 mN m^{-1}, which corresponds to the onset of the phase transition of pure core–shell particles,[53] a first phase transition was observed (Fig. 6b and f). Neighboring core–shell particles collapsed, while neither pure microgels nor mixed neighboring pairs were affected. This $PT_{low-low}$ phase transition is the analogue to the $PT_{small-small}$ in the previous case, where only the neighbor pairs with the smallest coronae collapse. In the binary monolayer with microgels as the major component, this phase transition causes the formation of dimers and trimers, which reflect the (limited) occasions where the minority core–shell particles came into direct contact. Above a surface pressure of 22 mN m^{-1}, microgels in contact with core–shell particles underwent a second phase transition ($PT_{high-low}$) and formed flower-like defect structures (Fig. 6c and g). The separation of these two phase transitions provides the opportunity to engineer defects with tailored shapes and structures within the hexagonal lattice formed by the non-collapsed microgel particles. Finally, at the highest surface pressures above 27 mN m^{-1}, the last phase transition ($PT_{high-high}$) occurred from collapsing large microgels pairs (Fig. 6d and h).

We also used the augmented ensemble simulation method to reproduce the experimentally observed phase transitions for the microgel–core–shell particle mixtures. Note that the simulations do not actually use a core–shell structure, but merely capture the facilitated phase transition by artificially reducing the stiffness of a uniform particle. For the sake of clarity in the comparison with the experiments, we nevertheless assign these particles as "core–shell". The simulated core–shell particles are thus represented by a uniform particle with the same size as the microgels in the expanded state ($\sigma_+ = 1.14$ μm), while it is larger

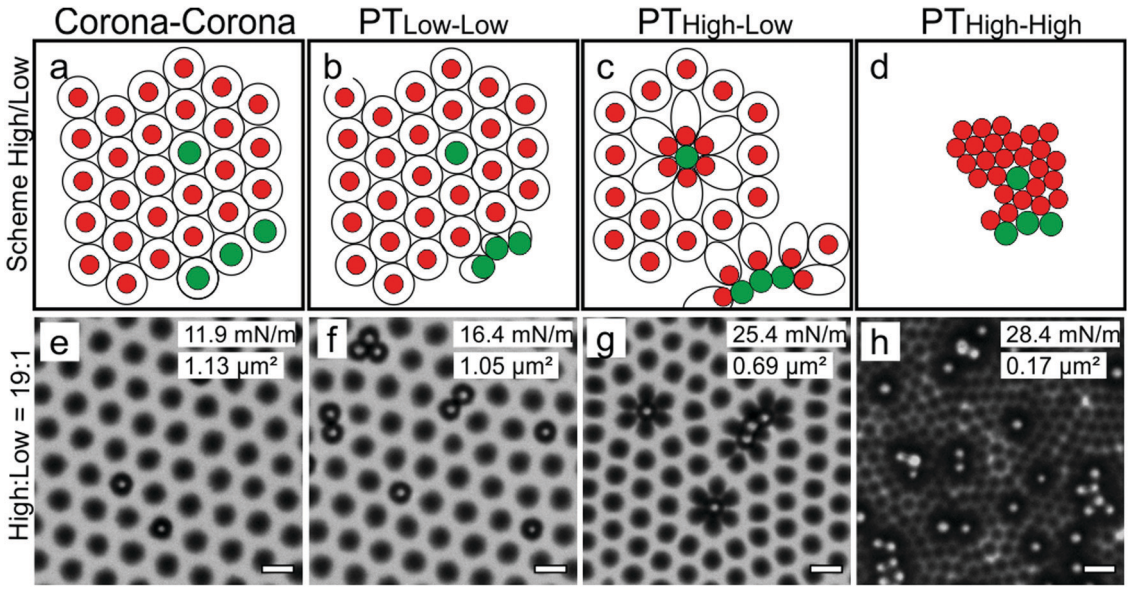

Fig. 6 Interfacial phase transition of mixtures of large microgels (2.5% crosslinker) and core–shell particles with similar dimensions in the expanded state. (a–d) Schematic representation of the hierarchy of phase transitions observed in the binary system. The phase transition of core–shell particles is denoted with the subscript "low", indicating their tendency to collapse at lower surface pressures. The phase transition of pure microgels is thus denoted as "high" since they collapse at higher surface pressures. (e–h) SEM images of the phase behavior upon increasing compression, showing the different phase transitions and the characteristic resulting defect structures. The mixing ratio between microgels and core–shell particles was 19 : 1. Surface pressure and particle area are displayed for each SEM image. Scale bar: 1 μm.

 This journal is © The Royal Society of Chemistry 2021

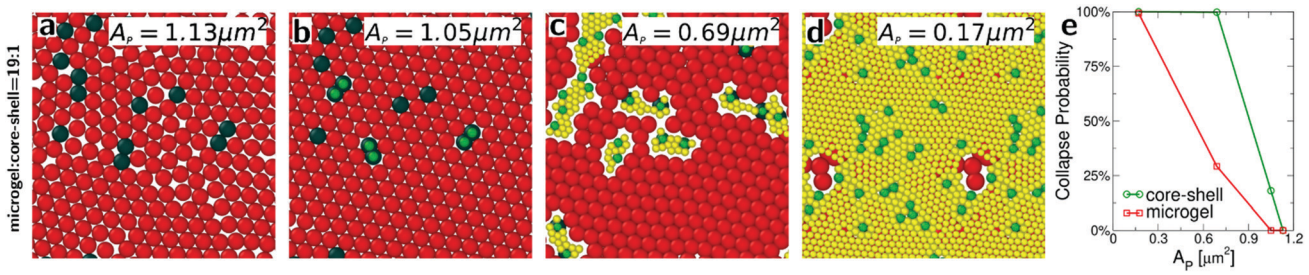

Fig. 7 Augmented ensemble simulations of a binary monolayer with different stiffnesses, mimicking the phase behavior of the experimental core–shell/microgel mixtures. Microgel particles are represented as red spheres that turn yellow upon collapse, while core–shell particles are simulated as green spheres with decreased stiffness to mimic their tendency to collapse at lower surface pressures. Core–shell particles turn from dark green to light green upon compression. The area per particle, A_p, decreases from a to d. In panel (c) we see the partial formation of flower-like defects, where the collapsed microgels (yellow) are localized around the core–shell particles. (e) Statistical evaluation of the phase transition upon compression showing the percentage of collapsed particles of both populations.

Published on 25 March 2021. Downloaded on 5/6/2021 2:20:36 PM.

in the collapsed state ($\sigma_- = 0.55$ μm). In line with the experiments, the collapse of the core–shell particles is facilitated in the simulations by increasing the stiffness parameter K, which is 1/10th of the microgels. Fig. 7 shows equilibrium snapshots of the simulations at different compressions. At low compression (large area per particle A_p), the binary mixture forms a hexagonal non-close packed configuration with high order, as expected from their identical sizes. With increasing compression, the neighboring core–shell particles are the first to collapse from corona–corona to core–core contacts, visualized by a change from a dark green to light green color (corresponding to the $PT_{low-low}$ in the experiments). Note that due to the low number of core–shell particles, only a few particle pairs collapse at this transition. With increasing compression, mixed pairs collapse in a second phase transition (corresponding to $PT_{high-low}$ in the experiments). In this regime, our simulations partially reproduce the characteristic flower-shaped defect structures observed experimentally, as can be seen in Fig. 7(c), where the collapsed microgels (yellow) are localized around the core–shell particles. It must be noted, however, that such flower-like defects are very hard to stabilize in our simulations. We attribute this to the fact that the formation of a flower structure requires all the petals to undergo a coordinated (multi-particle) collapse; while our simulation scheme does account for some multi-particle effects, we hypothesize that a full *in silico* description of the experimentally observed flower structures would require more advanced multi-body interactions (see Fig. S2, ESI†). For this reason most of our simulated flower structures lack the last petals and the collapsed core–shells (green) are not fully surrounded by collapsed microgels (yellow) in Fig. 7(c). Finally, at the highest compression, a final phase transition occurs where pure microgel pairs collapse ($PT_{high-high}$).

Discussion

Comparison to bulk behavior

In the bulk, defect self-healing is observed in soft microgel crystals consisting of small microgels with larger microgels as dopants, as the larger microgels shrink to fit into the lattice of the small microgels.[48–52] Scotti *et al.* rationalized the collapse of larger dopant microgels by the merging of microgel counter ion clouds and the resulting increase in osmotic pressure difference between the inside and the outside of the particles, forcing the water molecules to leave the network and causing a shrinkage of the larger microgel.[49,51,52] When adsorbed to the air/water interface, the microgels spread and deform into their characteristic core-corona morphology to decrease the overall interfacial energy.[23,28,59,60] At low surface pressures, they assemble into a hexagonal non-close-packed lattice, where they are in corona–corona contact.[61] A recent neutron reflectivity study revealed that the corona of the PNiPAm microgels adsorbed at the air/water interface consists of a nanometer thin film of highly stretched PNiPAm chains with a low water content, while the microgel core remained solvated.[26] Due to the low water content and the highly stretched polymer chains, the corona behaves differently compared to the microgel core or microgels in the bulk.[56] Thus, since the corona is already depleted of water, we rationalize that the osmotic pressure has little effect on the microgel corona and thus no self-healing in the 2D microgel crystals adsorbed at the air/water interface is observed. Similarly, variations in the charge of the microgel are not expected to significantly change the structure at the interface.[62]

Solid–solid phase transitions

We further observed no self-healing behavior when compressing the interfacially-confined binary microgel assembly. However, while monodisperse microgel systems involve a single solid–solid phase transition upon reaching a threshold surface pressure, binary microgel monolayers show three consecutive phase transitions, which we rationalized using three possible corona combinations: small–small, large–small, and large–large. This complex hierarchy of coronae collapses was also qualitatively captured by our simulations. The augmented potential method that we employed is naturally suited to model the mixtures we used in the experiments, since this method can explicitly account for the degree of corona collapse per particle. Interestingly, the defined hierarchy of the phase transitions also provides a means by which to control defect structures within the binary microgel lattices. In particular, characteristic "flower-like" defects arise from the preferred collapse of microgels surrounding core–shell

Published on 25 March 2021. Downloaded on 5/6/2021 2:20:36 PM.

particles with weaker corona structures. We note, however, that the formation of fully developed flower structures is relatively difficult to capture in simulations, since it requires a coordinated, multi-particle collapse of all "petals" comprising the defect. Future work should aim to identify a suitable many-body interaction potential that can mimic this defect phenomenology more accurately.

Conclusion

We investigated the interfacial phase behavior of binary microgel mixtures with different sizes. Compared to the behavior in the bulk where larger microgels partially collapse to fit into an ordered lattice of the majority population, no such structural re-arrangement was observed at the liquid interface and both populations maintained their individual interfacial morphologies, leading to disordered, binary monolayers. Upon compression, we observed a defined series of phase transitions with a clear hierarchy. First, at the lowest compression, neighboring particles with the smallest coronae undergo a phase transition into a close-packed arrangement. Subsequently, a mixed phase transition follows, where neighboring unequal pairs collapse. Finally, the microgel population with the most extended corona undergoes a phase transition to form a completely close-packed monolayer. The defined mixed phase transition allows for the local formation of characteristic, flower-like defects by introducing particles with "weaker" coronae as local nuclei for the phase transition. Overall, our study underlines the importance of the interfacial morphology and corona structure in understanding and control the phase behavior of soft, deformable particles at liquid interfaces.

Conflicts of interest

There are no conflicts to declare.

Acknowledgements

NV and HL acknowledge funding from the Deutsche Forschungsgemeinschaft (DFG) under grant numbers VO 1824/8-1 and LO 418/22-1, respectively. N. V. also acknowledges support from the Interdisciplinary Center for Functional Particle Systems (FPS). M. R. acknowledges funding from the Swiss National Science Foundation Project-ID P2SKP2_194953.

References

1 F. Wang, Z. Zheng, Y. Peng, Y. Han and Z. Wang, Imaging the homogeneous nucleation during the melting of superheated colloidal crystals, *Science*, 2012, **338**(6103), 87–90.
2 Y. Peng, F. Wang, Z. Wang, A. M. Alsayed, Z. Zhang, A. G. Yodh and Y. Han, Two-step nucleation mechanism in solid–solid phase transitions, *Nat. Mater.*, 2015, **14**(1), 101–108.
3 E. Allahyarov, K. Sandomirski, S. U. Egelhaaf and H. Lo, Crystallization seeds favour crystallization only during initial growth, *Nat. Commun.*, 2015, **6**, 7110.
4 Y. Peng, Z. Wang, A. M. Alsayed, A. G. Yodh and Y. Han, Melting of colloidal crystal films, *Phys. Rev. Lett.*, 2010, **104**(20), 19–22.
5 P. S. Mohanty, P. Bagheri, S. Nöjd, A. Yethiraj and P. Schurtenberger, Multiple path-dependent routes for phase-transition kinetics in thermoresponsive and field-responsive ultrasoft colloids, *Phys. Rev. X*, 2015, **5**(1), 1–8.
6 B. E. Vekris, V. Kitaev, D. D. Perovic, J. S. Aitchison and G. A. Ozin, Visualization of stacking faults and their formation in colloidal photonic crystal films, *Adv. Mater.*, 2008, 1110–1116.
7 B. P. V. Braun, S. A. Rinne and F. García-santamaría, Introducing defects in 3D photonic crystals: state of the art, *Adv. Mater.*, 2006, 2665–2678.
8 L. J. Bonales, F. Martínez-Pedrero, M. A. Rubio, R. G. Rubio and F. Ortega, Phase behavior of dense colloidal binary monolayers, *Langmuir*, 2012, **28**(48), 16555–16566.
9 P. Schall, I. Cohen, D. A. Weitz and F. Spaepen, Visualization of dislocation dynamics in colloidal crystals, *Science*, 2004, **305**, 1944–1949.
10 T. D. Edwards, Y. Yang, D. J. Beltran-villegas and M. A. Bevan, Formation and motion, *Sci. Rep.*, 2014, 1–8.
11 K. H. Nagamanasa, S. Gokhale, R. Ganapathy and A. K. Sood, Confined glassy dynamics at grain boundaries in colloidal crystals, *Proc. Natl. Acad. Sci. U. S. A.*, 2011, **108**(28), 1–4.
12 M. Chaudhuri, E. Allahyarov, H. Löwen, S. U. Egelhaaf and D. A. Weitz, Triple junction at the triple point resolved on the individual particle level, *Phys. Rev. Lett.*, 2017, **119**, 128001.
13 J. Wang, C. F. Mbah, T. Przybilla, B. A. Zubiri, E. Spiecker, M. Engel and N. Vogel, Magic number colloidal clusters as minimum free energy structures Junwei, *Nat. Commun.*, 2018, **9**, 5259.
14 V. N. Manoharan, M. T. Elsesser and D. J. Pine, Dense packing and symmetry in small clusters of microspheres, *Science*, 2003, **301**, 483–488.
15 R. McGorty, J. Fung, D. Kaz and V. N. Manoharan, Colloidal self-assembly at an interface, *Mater. Today*, 2010, **13**(6), 34–42.
16 D. M. Kaz, R. McGorty, M. Mani, M. P. Brenner and V. N. Manoharan, Physical ageing of the contact line on colloidal particles at liquid interfaces, *Nat. Mater.*, 2011, **11**(2), 138–142.
17 P. Pieranski, Two-dimensional interfacial colloidal crystals, *Phys. Rev. Lett.*, 1980, **45**(7), 569–572.
18 U. Gasser, C. Eisenmann, G. Maret and P. Keim, Melting of crystals in two dimensions, *ChemPhysChem*, 2010, 963–970.
19 N. Vogel, M. Retsch, C. A. Fustin, A. Del Campo and U. Jonas, Advances in colloidal assembly: The design of structure and hierarchy in two and three dimensions, *Chem. Rev.*, 2015, **115**(13), 6265–6311.
20 R. Aveyard, J. H. Clint, D. Nees and V. N. Paunov, Compression and structure of monolayers of charged latex particles at air/water and octane/water interfaces, *Langmuir*, 2000, **16**(4), 1969–1979.

 This journal is © The Royal Society of Chemistry 2021

Published on 25 March 2021. Downloaded on 5/6/2021 2:20:36 PM.

21 M. Karg, A. Pich, T. Hellweg, T. Hoare, L. A. Lyon, J. J. Crassous, D. Suzuki, R. A. Gumerov, S. Schneider, I. I. Potemkin and W. Richtering, Nanogels and microgels: From model colloids to applications, recent developments and future trends, *Langmuir*, 2019, **35**(19), 6231–6255.
22 H. Minato, M. Murai, T. Watanabe, S. Matsui, M. Takizawa, T. Kureha and D. Suzuki, The deformation of hydrogel microspheres at the air/water interface, *Chem. Commun.*, 2018, **54**(8), 932–935.
23 K. Geisel, L. Isa and W. Richtering, Unraveling the 3D localization and deformation of responsive microgels at oil/water interfaces: A step forward in understanding soft emulsion stabilizers, *Langmuir*, 2012, **28**(45), 15770–15776.
24 A. Rauh, M. Rey, L. Barbera, M. Zanini, M. Karg and L. Isa, Compression of hard core–soft shell nanoparticles at liquid–liquid interfaces: Influence of the shell thickness, *Soft Matter*, 2017, **13**(1), 158–169.
25 L. Scheidegger, M. Á. Fernández-Rodríguez, K. Geisel, M. Zanini, R. Elnathan, W. Richtering and L. Isa, Compression and deposition of microgel monolayers from fluid interfaces: Particle size effects on interface microstructure and nanolithography, *Phys. Chem. Chem. Phys.*, 2017, **19**(13), 8671–8680.
26 K. Zielińska, H. Sun, R. A. Campbell, A. Zarbakhsh and M. Resmini, Smart nanogels at the air/water interface: Structural studies by neutron reflectivity, *Nanoscale*, 2016, **8**(9), 4951–4960.
27 F. Camerin, M. Á. Fernández-Rodríguez, L. Rovigatti, M.-N. Antonopoulou, N. Gnan, A. Ninarello, L. Isa and E. Zaccarelli, Microgels adsorbed at liquid–liquid interfaces: A joint numerical and experimental study, *ACS Nano*, 2019, **13**(4), 4548–4559.
28 M. Rey, M. A. Fernandez-rodriguez, M. Karg, L. Isa and N. Vogel, Poly-*N*-isopropylacrylamide nanogels and microgels at fluid interfaces, *Acc. Chem. Res.*, 2020, **53**(2), 414–424.
29 M. Rey, M. Á. Fernández-Rodríguez, M. Steinacher, L. Scheidegger, K. Geisel, W. Richtering, T. M. Squires and L. Isa, Isostructural solid–solid phase transition in monolayers of soft core-shell particles at fluid interfaces: Structure and mechanics, *Soft Matter*, 2016, **12**(15), 3545–3557.
30 M. Rey, A. D. Law, D. M. A. Buzza and N. Vogel, Anisotropic self-assembly from isotropic colloidal building blocks, *J. Am. Chem. Soc.*, 2017, **139**(48), 17464–17473.
31 M. Rey, X. Hou, J. S. J. Tang and N. Vogel, Interfacial arrangement and phase transitions of PNiPAm microgels with different crosslinking densities, *Soft Matter*, 2017, **13**(46), 8717–8727.
32 A. S. El-Tawargy, D. Stock, M. Gallei, W. A. Ramadan, M. A. Shams El-Din, G. Reiter and R. Reiter, Multiple structural transitions in langmuir monolayers of charged soft-shell nanoparticles, *Langmuir*, 2018, **34**(13), 3909–3917.
33 S. Ciarella, M. Rey, J. Harrer, N. Holstein, M. Ickler, H. Lowen, N. Vogel and L. M. C. Janssen, Soft particles at liquid interfaces: From molecular particle architecture to collective phase behavior, *arxiv*, 2020, arXiv:2008.13695.
34 C. Picard, P. Garrigue, M. C. Tatry, V. Lapeyre, S. Ravaine, V. Schmitt and V. Ravaine, Organization of microgels at the air–water interface under compression: Role of electrostatics and cross-linking density, *Langmuir*, 2017, **33**(32), 7968–7981.
35 A. Scotti, S. Bochenek, M. Brugnoni, M. A. Fernandez-Rodriguez, M. F. Schulte, J. E. Houston, A. P. H. Gelissen, I. I. Potemkin, L. Isa and W. Richtering, Exploring the colloid-to-polymer transition for ultra-low crosslinked microgels from three to two dimensions, *Nat. Commun.*, 2019, **10**(1), 1418.
36 C. Picard, P. Garrigue, M.-C. Tatry, V. Lapeyre, S. Ravaine, V. Schmitt and V. Ravaine, Organization of microgels at the air–water interface under compression: Role of electrostatics and cross-linking density, *Langmuir*, 2017, **33**(32), 7968–7981.
37 N. Vogel, L. De Viguerie, U. Jonas, C. K. Weiss and K. Landfester, Wafer-scale fabrication of ordered binary colloidal monolayers with adjustable stoichiometries, *Adv. Funct. Mater.*, 2011, **21**, 3064–3073.
38 J. Yu, Q. Yan and D. Shen, Co-Self-assembly of binary colloidal crystals at the air–water interface, *Appl. Mater. Interfaces*, 2010, **2**(7), 1922–1926.
39 J. Wang, S. Ahl, Q. Li, M. Kreiter, T. Neumann, K. Burkert, W. Knoll and U. Jonas, Structural and optical characterization of 3D binary colloidal crystal and inverse opal films prepared by direct co-deposition, *J. Mater. Chem.*, 2008, **18**, 981–988.
40 J. Wang, Q. Li, W. Knoll and U. Jonas, Preparation of multilayered trimodal colloid crystals and binary inverse opals, *J. Am. Chem. Soc.*, 2006, **128**(49), 15606–15607.
41 K. P. Velikov, C. G. Christova, R. P. A. Dullens and A. Van Blaaderen, Layer-by-layer growth of binary colloidal crystals, *Science*, 2002, **296**(5565), 106–109.
42 H. Cong and W. Cao, Array patterns of binary colloidal crystals, *J. Phys. Chem. B*, 2005, **109**(5), 1695–1698.
43 A. Meller and J. Stavans, Glass transition and phase diagrams of strongly interacting binary colloidal mixtures, *Phys. Rev. Lett.*, 1992, **68**(24), 3646–3649.
44 J. M. Lynch, G. C. Cianci and E. R. Weeks, Dynamics and structure of an aging binary colloidal glass, *Phys. Rev. E: Stat., Nonlinear, Soft Matter Phys.*, 2008, **78**(3), 1–7.
45 L. Assoud, R. Messina and H. Löwen, Binary crystals in two-dimensional two-component Yukawa mixtures, *J. Chem. Phys.*, 2008, **129**, 164511.
46 L. Assoud, R. Messina and H. Löwen, Stable crystalline lattices in two-dimensional binary mixtures of dipolar particles stable crystalline lattices in two-dimensional binary mixtures of dipolar particles, *EPL*, 2007, **80**(4), 48001.
47 E. Fayen, A. Jagannathan, G. Foffi and F. Smallenburg, Infinite-pressure phase diagram of binary mixtures of (non) additive hard disks infinite-pressure phase diagram of binary mixtures of (non) additive hard disks, *J. Chem. Phys.*, 2020, **152**, 204901.
48 A. St, J. Iyer and L. A. Lyon, Self-healing colloidal crystals, *Angew. Chem., Int. Ed.*, 2009, **48**(25), 4562–4566.
49 A. Scotti, U. Gasser, E. S. Herman, M. Pelaez-Fernandez, J. Han, A. Menzel, L. A. Lyon and A. Fernández-Nieves, The role of ions in the self-healing behavior of soft particle

Published on 25 March 2021. Downloaded on 5/6/2021 2:20:36 PM.

suspensions, *Proc. Natl. Acad. Sci. U. S. A.*, 2016, **113**(20), 5576–5581.

50 A. Scotti, M. Brugnoni, A. A. Rudov, J. E. Houston, I. I. Potemkin and W. Richtering, Hollow microgels squeezed in overcrowded environments, *J. Chem. Phys.*, 2018, **148**, 174903.

51 U. Gasser, A. Scotti and A. Fernandez-Nieves, Spontaneous deswelling of microgels controlled by counterion clouds, *Phys. Rev. E*, 2019, **99**(4), 1–12.

52 A. Scotti, U. Gasser, E. S. Herman, J. Han, A. Menzel, L. A. Lyon and A. Fernandez-Nieves, Phase behavior of binary and polydisperse suspensions of compressible microgels controlled by selective particle deswelling, *Phys. Rev. E*, 2017, **96**(3), 1–14.

53 J. S. J. Tang, R. S. Bader, E. S. A. Goerlitzer, J. F. Wendisch, G. R. Bourret, M. Rey and N. Vogel, Surface patterning with SiO2@PNiPAm core–shell particles, *ACS Omega*, 2018, **3**(9), 12089–12098.

54 M. Rey, X. Hou, J. S. J. Tang and N. Vogel, Interfacial arrangement and phase transitions of PNiPAm microgels with different crosslinking density, *Soft Matter*, 2017, **13**(43), 8717–8727.

55 W. Stöber, A. Fink and E. Bohn, Controlled growth of monodisperse silica spheres in the micron size range, *J. Colloid Interface Sci.*, 1968, **26**(1), 62–69.

56 J. Harrer, M. Rey, S. Ciarella, H. Lö, L. M. C. Janssen and N. Vogel, Stimuli-responsive behavior of PNiPAm microgels under interfacial Confinement, *Langmuir*, 2019, **35**, 10512–10521.

57 H. J. C. Berendsen, J. P. M. Postma, W. F. van Gunsteren, A. DiNola and J. R. Haak, Molecular dynamics with coupling to an external bath, *J. Chem. Phys.*, 1998, **81**, 3684.

58 M. Moseler and P. Gumbsch, Structural relaxation made simple, *Phys. Rev. Lett.*, 2006, **97**(170201), 1–4.

59 H. Mehrabian, J. Harting and J. H. Snoeijer, Soft particles at a fluid interface, *Soft Matter*, 2016, **12**(4), 1062–1073.

60 R. W. Style, L. Isa and E. R. Dufresne, Adsorption of soft particles at fluid interfaces, *Soft Matter*, 2015, **11**(37), 1–8.

61 M. Rey, M. Á. Fernández-Rodríguez, M. Steinacher, L. Scheidegger, K. Geisel, W. Richtering, T. M. Squires and L. Isa, Isostructural solid–solid phase transition in monolayers of soft core–shell particles at fluid interfaces: Structure and mechanics, *Soft Matter*, 2016, **12**(15), 3545–3557.

62 M. M. Schmidt, A. A. Gavrilov, I. I. Potemkin and W. Richtering, Influence of charges on the behavior of polyelectrolyte microgels confined to oil–water interfaces, *Langmuir*, 2020, **36**(37), 11079–11093.

 This journal is © The Royal Society of Chemistry 2021